Monoclinic Tm:MgWO$_4$ crystal: Crystal-field analysis, tunable and vibronic laser demonstration

Pavel Loiko,[1,2] Yicheng Wang,[3] Josep Maria Serres,[1] Xavier Mateos,[1,*] Magdalena Aguiló,[1] Francesc Díaz,[1] Lizhen Zhang,[4] Zhoubin Lin,[4] Haifeng Lin,[4] Ge Zhang,[4] Elena Vilejshikova,[5] Elena Dunina,[6] Alexey Kornienko,[6] Liudmila Fomicheva,[7] Valentin Petrov,[3] Uwe Griebner,[3] and Weidong Chen[3,4,8]

[1]*Física i Cristal·lografia de Materials i Nanomaterials (FiCMA-FiCNA)-EMaS, Dept. Química Física i Inòrganica, Universitat Rovira i Virgili (URV), Campus Sescelades, E-43007 Tarragona, Spain*
[2]*ITMO University, 49 Kronverkskiy Pr., 197101 St. Petersburg, Russia*
[3]*Max Born Institute for Nonlinear Optics and Short Pulse Spectroscopy, Max-Born-Str. 2a, D-12489 Berlin, Germany*
[4]*Key Laboratory of Optoelectronic Materials Chemistry and Physics, Fujian Institute of Research on the Structure of Matter, Chinese Academy of Sciences, Fuzhou, 350002 Fujian, China*
[5]*Center for Optical Materials and Technologies (COMT), Belarusian National Technical University, 65/17 Nezavisimosti Ave., 220013 Minsk, Belarus*
[6]*Vitebsk State Technological University, 72 Moskovskaya Ave., 210035 Vitebsk, Belarus*
[7]*Belarusian State University of Informatics and Radioelectronics, 6 Brovka St., 220027 Minsk, Belarus*
[8]*chenweidong@fjirsm.ac.cn*
**Corresponding author e-mail: xavier.mateos@urv.cat*

ABSTRACT: Tm^{3+}-doped monoclinic magnesium monotungstate (MgWO$_4$) is a promising material for lasers emitting at above 2 µm. Stark splitting of $^3H_6$ to $^1G_4$ Tm^{3+} multiplets in MgWO$_4$ is determined using low-temperature spectroscopy, calculated within crystal-field theory modified for the case of an intermediate configuration interaction (ICI) and analyzed in terms of the barycenter plot. Tm^{3+}:MgWO$_4$ features a large Stark splitting of the ground-state ($^3H_6$), 633 cm^{-1}, and high transition cross-sections for polarized light due to its low-symmetry structure. A unique feature of Tm^{3+}:MgWO$_4$ to provide a naturally polarized emission at >2 µm, as well as its suitability for broadly tunable and mode-locked lasers in this spectral range are argued. The first tunable and vibronic Tm^{3+}:MgWO$_4$ lasers are demonstrated, yielding a continuous tuning from 1897 to 2062 nm in the former case. A vibronic laser operated at even longer wavelengths up to 2093 nm due to electron-phonon coupling with low-energy phonons of the crystalline host. Moreover, the optical indicatrix axes of high-refractive-index biaxial MgWO$_4$ are assigned.

Keywords: Tungstate crystals; Thulium ions; Stark splitting; Laser operation; Spectroscopy.

1. Introduction

Tungstate (oxide) crystals represent an important class of laser host materials suitable for doping with trivalent rare-earth ions (RE^{3+}). The most prominent examples are the monoclinic (sp. gr. $C2/c$) ordered double tungstates (DTs) [1] with chemical formula $KRE(WO_4)_2$, where RE = Gd, Y or Lu (shortly KREW), and the tetragonal scheelite-like (sp. gr. $I4_1/a$) disordered DTs [2] with chemical formula $LiRE(WO_4)_2$ or $NaRE(WO_4)_2$, where RE = Gd, Y, Lu or La (shortly LiREW or NaREW). Depending on the RE^{3+} dopant, the monoclinic DTs can be highly doped, e.g. with Yb^{3+} or Tm^{3+}, without change in their crystalline phase. They are characterized by high transition cross-sections for polarized light and broad emission bands [1]. Their tetragonal counterparts feature additional inhomogeneous line broadening [2]. These properties make the DTs very suitable for the development of highly-efficient continuous-wave (CW) [3,4] and especially mode-locked (ML) near-IR lasers [5,6]. The main limitation of the DTs is their moderate thermal conductivity, namely ~3 W/mK for the monoclinic crystals [1] and even ~1 W/mK for the tetragonal ones, leading to strong thermo-optic effects promoted by the negative dn/dT. This disadvantage is partially compensated by a strongly anisotropic thermal expansion allowing for the so-called “athermal” behavior [7].

Besides the DTs, the divalent-metal monotungstates, $M^{2+}WO_4$, are also known as laser crystalline hosts. During the past decades, the main attention was paid to the tetragonal scheelite ($CaWO_4$) type phase observed for M = Ca, Sr, Ba, or Pb. Barely used as RE^{3+}-doped laser materials, these crystals were found to be very suitable for Raman shifters [8]. Their thermal conductivity is moderate, ~3 W/mK. When tetragonal MWO_4 crystals are doped with RE^{3+} ions, the latter replace the M^{2+} cations. Both the mismatch of the ionic radii and the necessity of a charge compensation limit the RE^{3+} doping level [9], while the structure of the tetragonal MWO_4 crystals does not provide large transition cross-sections for the RE^{3+} ions. Moreover, dn/dT is negative for the tetragonal MWO_4 crystals whilst its detrimental effect typically cannot be compensated by the thermal expansion. The RE^{3+}-doped tetragonal monotungstates $M^{2+}WO_4$ synthesized in the form of nano- and micro-crystals are attractive for applications as phosphors [10-12].

There exist also monoclinic (same sp. gr. $P2/c$) divalent-metal monotungstates, $M^{2+}WO_4$, where M = Mg, Cu, Ni, Co, Fe, Zn, Mn or Cd [13-16]. In particular, the structure of the monoclinic magnesium tungstate, $MgWO_4$ was reported in [17]. Great efforts were dedicated to the synthesis of nanocrystals and ceramics based on monoclinic $M^{2+}WO_4$ phases in recent years [18-20]. In earlier work, single-crystal $MgWO_4$ was studied as a scintillator [21,22]. Later on, it was considered as a host for transition-metal ions, e.g. Cr^{3+}, featuring very broad emission bands in the near-IR [23] but laser operation with $Cr:MgWO_4$ has not been achieved yet. Recently, $MgWO_4$ was proposed as a suitable host for the RE^{3+} ions. Initial work focused on $Yb:MgWO_4$, leading to laser action under diode-pumping with an output power of 2.52 W at 1060 nm and slope efficiency η of 53% [24]. The $Yb:MgWO_4$ crystal was also employed for optical vortex laser beam generation [25]. Tuning of a $Yb:MgWO_4$ laser between 1019 and 1067 nm was reported [26]. The room-temperature spectroscopy and laser operation of $Tm:MgWO_4$ were first reported in [27]. A diode-pumped $Tm:MgWO_4$ laser generated 3.09 W at 2022-2034 nm with $\eta = 50\%$ [28].

The advantage of $MgWO_4$ is its high thermal conductivity of ~8.7 W/mK as measured for an arbitrary crystal orientation [29]. A positive thermal lens occurred for some crystal cuts as confirmed by the microchip laser operation [28] in a plano-plano cavity. The mismatch of the ionic radii of the RE^{3+} ions and the Mg^{2+} cations together with the low-symmetry structure promote broad and intense spectral bands both in absorption and emission [24,27]. The latter property was successfully exploited in ML lasers. A diode-pumped Yb:$MgWO_4$ laser ML by a Semiconductor Saturable Absorber Mirror, SESAM generated 125 fs-long pulses at 1065 nm at a repetition rate of 117 MHz [26]. A Ti:Sapphire laser-pumped Tm:$MgWO_4$ laser ML by a graphene saturable absorber generated 86 fs pulses at 2017 nm at a repetition rate of 87 MHz nm featuring an emission bandwidth of 53 nm [30]. These are the shortest pulses ever achieved with a bulk ML laser at ~2 μm.

In this work, we study the Tm:$MgWO_4$ crystal to demonstrate its exceptional suitability for lasers emitting at wavelengths slightly above 2 μm, by resolving the Stark splitting of the Tm^{3+} ion and demonstrating tunable and vibronic CW laser operation. This work is motivated by the potential applications of the eye-safe emission ($^3F_4 \rightarrow {}^3H_6$) of Tm lasers in remote sensing (LIDAR), spectroscopy and medicine.

2. Crystal structure and optical indicatrix

2.1. Crystal structure

The Tm:$MgWO_4$ crystal is monoclinic (centrosymmetric point group 2/*m*, space group C^4_{2h} – *P*2/*c*, No. 13). The host material, $MgWO_4$, is called huanzalaite in mineral form. It belongs to the family of monoclinic divalent-metal monotungstates with a wolframite [(Fe,Mn)WO_4] type structure. For 0.89 at. % Tm:$MgWO_4$, the lattice constants are a = 4.697 Å, b = 5.678 Å, c = 4.933 Å (Z = 2), and angle $\beta = \boldsymbol{a}$^$\boldsymbol{c}$ is 90.77° [27]. The cleavage plane of $MgWO_4$ is (010).

The structure of $MgWO_4$ is presented in Fig. 1 (according to the atomic coordinates from [17]). The Mg^{2+} cations (2*f* Wyckoff positions) are VI-fold O^{2-} coordinated, the Mg-O distances in the distorted [MgO_6] octahedra are 2.03-2.09 Å. The W^{6+} cations (*2e* Wyckoff positions) are also located in distorted octahedra with W-O distances of 1.82-2.10 Å. The network of $MgWO_4$ is formed by alternating zig-zag chains of edge-sharing [MgO_6] and [WO_6] polyhedra along the ***c***-axis, see Fig. 1(b,c). The Mg-Mg distances are 3.06 Å. In the ordered $MgWO_4$ structure, there is only a single site for Mg^{2+} ions despite the information published in [28]. The corresponding molybdate compound, $MgMoO_4$, can exist in several forms but is typically found to be monoclinic with a space group C^3_{2h} - *C*2/*m*, No. 12 (*β*-phase, sanmartinite [(Zn,Fe)WO_4] type, Z = 8) [21]. For this phase, two non-equivalent sites for the Mg^{2+} cations (4*g* and 4*i* Wyckoff positions) are present [21].

When $MgWO_4$ is doped with RE^{3+} ions, they are expected to substitute for the Mg^{2+} ones. The local symmetry of the latter is C_2 [15]. The ionic radii of Mg^{2+} and Tm^{3+} for a coordination number (C.N.) of VI are R_{Mg} = 0.72 Å and R_{Tm} = 0.88 Å, respectively. Such a big difference additionally distorts the [Mg/TmO_6] polyhedra, i.e. the Mg/Tm-O distances, according to our preliminary analysis of the X-ray diffraction pattern of Tm:$MgWO_4$ reported in [27]. The charge compensation is expected to be provided by the Na^+ ions entering from the flux during the crystal growth. Still, a single site for the RE^{3+} ions in $MgWO_4$ is expected, as confirmed by a clearly single-exponential luminescence decay of Yb^{3+} and Tm^{3+} in $MgWO_4$ [24,27]. The large difference of ionic radii of the substituted (Mg^{2+}) and the optically active (Tm^{3+}) ions, as well as the presence of large Na^+

ions acting as change compensators (ionic radius: 1.02 Å for C.N. = VI) are expected to determine strong distortion of the crystal-field for Tm^{3+} ions leading to large Stark splitting and broad spectral bands. Further conclusions about the role of Na^{+} ions and the possible presence of vacancies can be obtained from the Rietveld analysis.

2.2. Optical indicatrix

In the present work, we studied a 0.89 at.% Tm:$MgWO_4$ crystal (measured $N_{Tm} \approx 1.41\times10^{20}$ cm^{-3}) grown by the Top Seeded Solution Growth (TSSG) method using sodium tungstate, Na_2WO_4, as a solvent [27]. The monoclinic $MgWO_4$ is optically biaxial. Its optical properties are then described in the optical indicatrix frame with the three mutually orthogonal dielectric axes. One of them is parallel to the ***b***-axis (C_2 axis) while the other two are rotated around this axis with respect to the crystallographic ***a*** and ***c*** axes. The values of the refractive indices of $MgWO_4$ corresponding to the principal light polarizations are unknown. Because of the unknown refractive indices, in the previous papers, the optical indicatrix axes of $MgWO_4$ were arbitrarily denoted as X, Y and Z [24,27] and the Y-axis was selected to be parallel to the C_2 axis. The refractive indices were claimed to be high and exhibit a notable birefringence in [31]. In [32], the medium refractive index was assigned to polarization parallel to the ***b*** axis.

In order to gain more clarity with respect to the refractive indices, we studied the optical transmission of a laser quality polished 3×3×3 mm^3 cube of 1.25 at.% Yb:$MgWO_4$ oriented by transmission measurements with a polarizing microscope along the three dielectric axes [24]. We measured the transmission in the ~1.2 μm transparency range with polarized light using a Varian CARY 5000 spectrophotometer. The obtained values of the refractive indices are $n_p = 1.97$, $n_m = 2.03$ and $n_g = 2.13\pm0.02$ according to the $n_p < n_m < n_g$ convention widely used for biaxial laser crystals [1]. The orientation of the corresponding optical indicatrix axes $\{N_p, N_m, N_g\}$ is shown in Fig. 2. With respect to the {X, Y, Z} notations used previously [24,27], the assignment is the following: Z = N_p, Y = N_m and X = N_g. The rotation angles at room temperature are $\varphi = \boldsymbol{a}$^N_g = 36.4° and $\psi = \boldsymbol{c}$^N_p = 37.1°. The angle between the two optic axes $2V_g$ amounts to 78.8° and thus $MgWO_4$ is a positive biaxial crystal. The optical axes are located in the N_p-N_g (***a***-***c***) plane.

3. Optical spectroscopy

3.1. Stark splitting of the energy levels

To determine the Stark splitting of the Tm^{3+} multiplets in $MgWO_4$, we measured the low-temperature (LT, at 6 K) absorption and emission spectra. In the latter case, the $^3H_4 \rightarrow {}^3H_6$ (at ~0.8 μm) and $^3F_4 \rightarrow {}^3H_6$ (at ~2 μm) luminescence was monitored. The measurements were performed for two light polarizations, $\boldsymbol{E} \parallel N_g$ and $\boldsymbol{E} \parallel N_m$, e.g., for light polarized perpendicular and parallel to the ***b***-axis ($\boldsymbol{b} \parallel C_2$), respectively, because the polarization selection rules for the RE^{3+} ions in the C_2 sites are different for these polarizations. The spectra were interpreted considering a total of $2J+1$ Stark sub-levels for any multiplet.

The polarized LT absoption and emission spectra of Tm:$MgWO_4$ are shown in Fig. 3 and Fig. 4, respectively. The absorption lines measured at 6 K for Tm^{3+} in $MgWO_4$ are much broader than those in KLuW [33] indicating stronger crystal-field.

The experimental energies of the Stark sub-levels E_{exp} of the $^3H_6$ to $^1G_4$ Tm^{3+} multiplets are listed in Table 1.

Fig. 5(a) shows the energy-level scheme of Tm^{3+} in $MgWO_4$, as well as the relevant spectroscopic processes. In Fig. 5(b), we compared the Stark splitting of the ground-state, $^3H_6$, and the upper laser level, $^3F_4$, of Tm^{3+} in monoclinic $MgWO_4$, monoclinic KLuW [33] and tetragonal NaGdW [2] crystals. The total Stark splitting of the ground-state, $\Delta E(^3H_6)$, is 633 cm^{-1} for Tm:$MgWO_4$, and it is larger compared to Tm:KLuW (530 cm^{-1}) and Tm:NaGdW (373 cm^{-1}) [2,33]. This larger splitting is attributed to the lower C.N. for Tm^{3+} ions in $MgWO_4$ (VI) in comparison to the two DTs (VIII), as well as to a larger difference between the ionic radii of the passive and the dopant ions in $MgWO_4$. The total Stark splitting of the upper laser level, $\Delta E(^3F_4)$ = 520 cm^{-1}, is also larger for Tm:$MgWO_4$. The transition between the lowest Stark sub-level of the $^3F_4$ state (5591 cm^{-1}) to the upper sub-level of the $^3H_6$ state (633 cm^{-1}) corresponding to the longest wavelength of a purely electronic transition occurs at 2017 nm for Tm:$MgWO_4$. This wavelength is much longer compared to Tm:KLuW (1948 nm) and Tm:NaGdW (1915 nm).

To calculate the position of the Stark sub-levels of the Tm^{3+} ions, the crystal-field theory has been applied. For a phenomenological description of the crystal-field splitting of the multiplets ($^{2S+1}L_J$) of the RE^{3+} ions, the following hamiltonian of the crystal field is typically used:

$$H_{CF} = \sum_k \sum_{q=-k}^{k} B_q^k C_q^k, \text{ where } C_q^k = \sum_{i=1}^{N} c_q^k(i). \tag{1}$$

Here, C^k_q is the spherical tensor operator and the parameters of the crystal field B^k_q are considered as free fitting parameters or they are calculated according to some microscopic theory. Further calculations depend on the choice of basis functions which are used for the calculation of the H_{CF} matrix. For the so-called weak configuration interaction (WCI) approximation, these functions are selected only within the $4f^n$ configuration. Then, the set of B^k_q parameters should be the same for all $4f^n$ multiplets.

For an intermediate configuration interaction (ICI) approximation, the generalized crystal-field parameters $(B^k_q)_{\mathrm{tot}}$ are dependent on the multiplet energy according to a linear law [34]:

$$H_{CF} = E_{\gamma J}\delta_{\gamma JM,\gamma' J' M'} + \sum_k \sum_{q=-k}^{k} (B_q^k)_{\mathrm{tot}}\ C_q^k, \tag{2a}$$

$$\text{where } (B_q^k)_{\mathrm{tot}} = B_q^k + \left(E_{\gamma J} + E_{\gamma' J'}\right) G_q^k. \tag{2b}$$

Here, the Kronecker delta δ_{ij} is used. In Eq. (2), the parameters B^k_q and the parameters of the configuration interaction G^k_q determine the amplitude of two terms with different dependence law on the multiplet energy. This allows to determine both sets of parameters (B^k_q and G^k_q) unambiguously from the optical spectra. Here, $G^k_q = G^k_q(d) + G^k_q(c)$ where the two contributions represent the influence of mixing of states with an excited configuration of opposite parity and configurations with charge transfer, respectively.

An admixture of excited configurations of opposite parity is mostly provided by the crystal field with odd symmetry. Thus, the value of $G^k_q(d)$ depends on the parameters of crystal field with odd symmetry $B^p_q(d)$ [35]:

$$G_q^k(d) = -\frac{2k+1}{2\left\langle f \middle\| c^k \middle\| f \right\rangle} \sum_{p',p''} \sum_{t',t''} (-1)^q (..)\{..\} \left\langle f \middle\| c^{p'} \middle\| d \right\rangle \left\langle d \middle\| c^{p''} \middle\| f \right\rangle \frac{B_{t'}^{p'}(d)}{\Delta_d} \frac{B_{t''}^{p''}(d)}{\Delta_d}, \tag{3a}$$

where $(..)=\begin{pmatrix} p' & p'' & k \\ t' & t'' & -q \end{pmatrix}$, and $\{..\}=\begin{Bmatrix} p' & p'' & k \\ f & f & d \end{Bmatrix}$. (3b)

Here, f and d are the orbital quantum numbers of electrons, (..) and {..} are the 3j an 6j symbols, respectively, $\langle f\|c^k\|f\rangle$, $\langle f\|c^{p'}\|d\rangle$ and $\langle d\|c^{p'}\|f\rangle$ are non-zero reduced matrix elements of one-electron spherical tensor (only for even $f+k+f$, $f+p'+d$ and $d+p''+f$, respectively), and Δ_d is the energy of the excited configuration. These matrix elements are determined as follows [36]:

$$\left\langle l\left\|c^k\right\|l'\right\rangle=(-1)^l\sqrt{(2l+1)(2l'+1)}\begin{pmatrix} l & k & l' \\ 0 & 0 & 0 \end{pmatrix}. \tag{4}$$

The terms $G^k_q(c)$ related to the charge transfer depend on the covalence parameters $\gamma_{\sigma f}$ and $\gamma_{\pi f}$ [36]:

$$G_q^k(c)=\sum_b J^k(b)C_q^{k*}(\Theta_b,\Phi_b), \tag{5}$$

where, the spherical harmonic C^k_q depends on the angles Θ_b and Φ_b indicating the direction to the ligand b. The parameters $J^k(b)$ can be calculated as follows [36]:

$$\tilde{J}^2(b)\approx\frac{5}{28}\left[2\gamma_{\sigma f}^2+3\gamma_{\pi f}^2\right],\ \tilde{J}^4(b)\approx\frac{3}{14}\left[3\gamma_{\sigma f}^2+\gamma_{\pi f}^2\right],\ \tilde{J}^6(b)\approx\frac{13}{28}\left[2\gamma_{\sigma f}^2-3\gamma_{\pi f}^2\right]. \tag{6}$$

Thus, the use of Eqs. (2)-(6) allows one to determine not only the parameters of the crystal field B^k_q and the parameters of the configuration interaction $G^k_q(d)$ and $G^k_q(c)$, but also the parameters of the crystal field with odd symmetry $B^p_q(d)$ and the covalency parameters $\gamma_{\sigma f}$ and $\gamma_{\pi f}$.

The calculated energies of the Stark sub-levels E_{calc} of the Tm^{3+} multiplets in $MgWO_4$ are listed in Table 1. The results obtained with Eq. (1) (WCI model) and Eqs. (2)-(6) (ICI model) are presented. The latter approach provides lower standard deviation between E_{exp} and E_{calc} (σ = 28.8 cm^{-1}, compare with σ = 42.7 cm^{-1} for WCI model).

The parameters of the hamiltonian of the crystal field calculated within the WCI and ICI approximations are listed in Table 2.

For RE^{3+} ions, the barycenter of any $^{2S+1}L_J(4f^n)$ multiplet shows a linear variation with the barycenter of any other isolated $4f^n$ multiplet which is expressed as a barycenter plot [37]. We used this rule to evaluate the assignment of the Stark sub-levels of Tm^{3+} in $MgWO_4$: We plotted the barycenter of the upper laser level, $\langle E\rangle(^3F_4)$, vs. that of the ground-state, $\langle E\rangle(^3H_6)$, Fig. 6(a). Neglecting the J-mixing, the energy separation between the two barycenters should be constant and equal to the corresponding separation for the free Tm^{3+} ion (~5600 cm^{-1}) [38]. Together with $Tm:MgWO_4$, we analyzed several Tm^{3+}-doped crystals; the corresponding Stark splitting can be found elsewhere. The least-square fit of the data in Fig. 6(a) yields a linear dependence $\langle E\rangle(^3F_4)$ = 5571 + 1.00·$\langle E\rangle(^3H_6)$ cm^{-1} clearly supporting the barycenter law. The multiplet barycenters for Tm^{3+} in $MgWO_4$ agree well with a general trend in Fig. 6(a).

In Fig. 6(b), the energy separation between the lowest Stark sub-level of the $^3F_4$ state and the upper sub-level of $^3H_6$ is plotted as $E_{min}(^3F_4$-$^3H_6)$ vs. the total Stark spitting ΔE of the $^3H_6$ ground-state for various Tm^{3+}-doped laser crystals. The isostructural crystals are denoted by the same symbol. In general, an increase of $\Delta E(^3H_6)$ leads to a decreased $E_{min}(^3F_4$-$^3H_6)$ and, consequently, to the capability to emit at longer wavelengths. Values of $E_{min}(^3F_4$-$^3H_6)$ < 5000 cm^{-1} (emission at >2 μm) are normally observed for two crystal families: cubic sesquioxides, RE_2O_3, where RE = Y, Lu or Sc, and cubic garnets, $RE_3A_5O_{12}$ (shortly REAG) where RE = Y, Lu or Gd and A = Al or Ga.

The cubic crystal structure determines an unpolarized laser output unless a polarization-sensitive element is inserted into the laser cavity. A variety of anisotropic crystals offering naturally polarized laser emission, e.g., tetragonal YLF, NaGdW and YVO_4, monoclinic KLuW, etc., normally provide Tm^{3+} laser emission at <2 μm. The $Tm:MgWO_4$ occupies an intermediate position offering laser emission slightly above 2 μm.

3.2. Stimulated-emission cross-sections

The stimulated-emission (SE) cross-sections σ_{SE} for the $^3F_4 \rightarrow {}^3H_6$ transition of Tm^{3+} in $MgWO_4$ were calculated using two methods. The first one was the reciprocity method (RM) [39]:

$$\sigma^i_{\mathrm{SE}}(\lambda) = \sigma^i_{\mathrm{abs}}(\lambda)\frac{Z_1}{Z_2}\exp(-\frac{hc/\lambda - E_{\mathrm{ZPL}}}{kT}), \tag{7a}$$

$$Z_m = \sum_k g^m_k \exp(-E^m_k / kT). \tag{7b}$$

where σ^i_{abs} is the absorption cross-section for the i-th polarization, h is the Planck constant, k is the Boltzmann constant, T is the crystal temperature (RT), E_{ZL} is the energy difference between the lowest Stark sub-levels of the two multiplets (zero phonon line (ZPL), 5591 cm^{-1}, Fig. 5(b)), and Z_m are the partition functions of the lower ($m = 1$) and upper ($m = 2$) manifolds. g^m_k (assumed to be 1) is the degeneracy of the sub-level with the number k and energy E^m_k measured from the lowest sub-level of the multiplet, Fig. 5(b). For Tm^{3+} in $MgWO_4$, $Z_1 = 4.36$ and $Z_2 = 3.93$, so that $Z_1/Z_2 = 1.11$ (cf. the values calculated for KLuW and NaGdW and shown in Fig. 5(b)).

The second method used the Füchtbauer–Ladenburg (F-L) equation [40]:

$$\sigma^i_{\mathrm{SE}}(\lambda) = \frac{\lambda^5}{8\pi n_i^2 \tau_{\mathrm{rad}} c}\frac{3W_i(\lambda)}{\sum\limits_{i=p,m,g}\int \lambda W_i(\lambda)\mathrm{d}\lambda}, \tag{8}$$

where $W_i(\lambda)$ is the measured luminescence spectrum for the i-th polarization [27], τ_{rad} is the radiative lifetime of the emitting state ($^3F_4$), which amounts to 1.95 ms according to the Judd-Ofelt modelling [27], and c is the speed of light. The results are shown in Fig. 7(a). Here, we consider the high-gain light polarization N_m. The SE cross-section spectra obtained by the two methods are in good agreement with each other indicated by the accuracy of the τ_{rad} value. According to the RM, the maximum σ_{SE} amounts to 2.8×10^{-20} cm^2 at 1878 nm.

The Tm^{3+} ion represents a quasi-three-level scheme exhibiting reabsorption and thus the gain cross-sections, $\sigma_g = \beta\sigma_{SE} - (1-\beta)\sigma_{abs}$, are calculated to predict the laser wavelength, see Fig. 7(b). Here, $\beta = N_2(^3F_4)/N_{Tm}$ is the inversion ratio and the σ_{SE} values calculated by the RM are used. The feature of $Tm:MgWO_4$ is that for $\beta < 0.25$ the gain cross-section spectrum is smooth and broad, showing a local peak centered at ~2017 nm. The SE cross-section at this wavelength is 1.0×10^{-20} cm^2. For $\beta = 0.2$, the gain bandwidth is ~80 nm (FWHM).

4. Tunable laser operation

4.1. Laser set-up

An X-shaped laser cavity was employed, Fig. 8. It consisted of two concave dichroic folding mirrors M1 and M2 coated for high transmission (HT) at 0.77-1.05 μm and for high reflectivity (HR) at 1.8-2.1 μm (radius of curvature $R = 100$ mm), a flat rear mirror M3 coated for HR at 1.9-2.2 μm and a flat wedged (~5') output coupler (OC) with transmission T_{OC} = 0.5%, 1.5%, 3% or

5% at 1.8-2.1 μm. The M1 and M2 mirrors were placed at a separation of 10 cm. The total geometrical cavity length was 150 cm. The two cavity arms were nearly balanced with 70 cm length each benefiting from the extended stability range with respect to the tolerated separation of the curved mirrors. A 3 mm-thick uncoated 0.89 at.% Tm:$MgWO_4$ crystal was placed at Brewster angle between the folding mirrors M1 and M2. It was oriented for propagation along the N_g axis, N_m-polarization. The crystal was wrapped in In-foil to improve the thermal contact and mounted in a water-cooled Cu-holder (temperature: 14 °C). Wavelength tuning was studied by inserting a 3.2 mm-thick quartz plate with the optical axis at 60° to the surface close to the OC.

The laser crystal was pumped through M1 in a single pass by a CW Ti:Sapphire laser tuned to 792 nm ($^3H_6 \rightarrow ^3F_4$ transition of Tm^{3+}, $\sigma_{abs} = 1.43\times10^{-20}$ cm^2 for $E \parallel N_m$) which delivered up to 4.1 W of pump power. The pump radiation was focused by a 70 mm spherical lens. The pump spot radius w_p in the crystal was 30 μm. At an incident pump power of 3.9 W, the absorption under lasing conditions was 44.1%, 44.9%, 43.5%, 42.1% for the four studied OCs, respectively. These values indicate certain absorption bleaching and absorption recovery depending on the intracavity power. The calculated low-signal absorption amounts to 49%.

4.2. Laser performance

Initial laser experiments were performed without the Lyot filter, Fig. 9(a). The maximum output power was achieved for T_{OC} = 3%, namely 0.58 W at 2019 nm with a slope efficiency η of 35.5% (vs. the absorbed pump power P_{abs}). The laser threshold was at P_{abs} = 80 mW. For higher T_{OC} of 5%, the laser output deteriorated (η = 34%) due to the upconversion losses caused by the higher inversion. Typical laser emission spectra are shown in Fig. 9(b). With the increase of T_{OC}, the peak emission wavelength experienced a blue-shift from 2024 to 2018 nm. This behavior is in line with the gain spectra, Fig. 7(b), and is related to the quasi-three-level nature of the Tm^{3+} ion.

The tuning curve of the Tm:$MgWO_4$ laser is shown in Fig. 9(c) (for T_{OC} = 1.5%). The laser was continuously tuned from 1897 to 2062 nm (a total tuning range of 165 nm). At longer wavelengths, the power dropped to zero partly due to the Lyot filter transmission. A maximum output power of 0.47 W was achieved at 2027 nm. In Fig. 9(c), the tuning curve for a 3.7 at.% Tm:KLuW crystal in a similar laser set-up [1] is also shown. The crystal was N_g-cut and used for N_p-polarization. For the Tm:KluW laser, the total tuning range was 186 nm (from 1800 to 1986 nm), confined to wavelengths below 2 μm.

5. Vibronic laser operation

5.1. Laser set-up

Vibronic laser operation was studied in a microchip-type laser set-up [41]. A rectangular 0.89 at.% Tm:$MgWO_4$ crystal with dimensions 1.86(N_g)×3.96(N_m)×3.05(N_p) mm^3 was used. All crystal faces were polished to laser quality and remained uncoated. Two crystal orientation were studied, N_g- and N_p-cut, both giving access to the N_m-polarization. The crystal was mounted to provide good thermal contact from all 4 lateral sides in a holder which was water-cooled at 12 °C.

The laser cavity consisted of a flat pump mirror (PM) that was coated for HT at 0.8–1.0 μm and HR at 1.8–2.15 μm and a flat "bandpass" OC with HT (> 80%) at 1.9–1.97 μm and T_{OC} = 1.6% at 2.05–2.20 μm. Both PM and OC were placed close to the crystal to reduce the intracavity losses.

The crystal was pumped by an AlGaAs fiber-coupled laser diode (fiber core diameter: 200 μm, numerical aperture, N.A. = 0.22). The pump wavelength (802 nm) was controlled by water-cooling of the laser diode. The unpolarized pump radiation was collimated and focused into the crystal using a lens assembly (1:1 reimaging ratio, 30 mm focal length). The pump spot radius in the laser crystal w_P was 100 μm and the confocal parameter $2z_R$ was 1.8 mm. The crystal was pumped again in a single-pass and the absorption under lasing conditions amounted to 14% (N_g-cut) and 36% (N_p-cut) being weakly dependent on the pump level.

5.2. Laser performance

Laser operation in the microchip cavity with the "bandpass" OC was achieved for both the N_g and N_p crystal cuts due to the positive thermal lens [28]. The laser output was linearly polarized along the N_m-axis; the polarization was naturally selected by the anisotropy of the gain. Microchip laser operation for the N_m-cut crystal was not achieved because of the negative sign of the thermal lens. This indicates negative dn/dT coefficients in $MgWO_4$ and thus the possibility of "athermal" behaviour for certain crystal cuts.

The input-output dependences of the vibronic laser are shown in Fig. 10(a). For the N_p-cut, the maximum output power was 0.75 W at 2043-2093 nm with η = 23%. The laser threshold was at P_{abs} = 0.25 W. For P_{abs} > 3 W, a thermal roll-over was observed. For the N_g-cut, a very similar output performance was observed (η = 22%), while power scaling was limited by the low pump absorption to 0.26 W at 2034-2053 nm. Typical laser emission spectra are shown in Fig. 10(b). They contain multiple peaks due to the etalon (Fabry-Perot) effects at the crystal-mirror interfaces. For the N_g-cut crystal, the mean emission wavelength was shorter than that for the N_p-cut one due to the smaller crystal thickness along the former direction. The latter leads to weaker reabsorption and also reduced the efficiency of the vibronic interaction. The observation of laser emission up to 2093 nm indicates the feasibility of further spectral tuning of the $Tm:MgWO_4$ lasers.

The longest wavelength of a purely electronic transition for $Tm:MgWO_4$ is 2017 nm, Fig. 5(b). Thus, the emission in Fig. 10(b) is due to a coupling of electrons that participate in the electronic transition $^3H_6 \rightarrow {}^3F_4$, with low-energy phonons of the host (vibronic coupling). The relaxation of a Tm^{3+} ion from the $^3F_4$ state may lead to the excitation of a phonon with an energy $h\nu_{ph}$ and emission of a photon with lower energy $\Delta E^* = \Delta E - h\nu_{ph}$ (longer wavelength) than expected from a purely electronic transition ΔE. This can be described in terms of a virtual energy level obtained by adding $h\nu_{ph}$ to the energy of the upper Stark sub-levels of the $^3H_6$ ground state [41], so that the transition from the $^3F_4$ state terminates at one of the virtual states. The Raman spectra of $Tm:MgWO_4$ were measured in [27]. This crystal exhibits several low-energy external modes at 98 (B_g), 121 (A_g) and 134 (B_g) cm^{-1}. These modes are responsible for the observed vibronic emission.

In Table 3, the output characteristics of the vibronic Tm lasers repored so far [41-45] are compared. The general trend is that the crystals with high Tm^{3+} doping do not require a special "bandpass" OC but just a broadband OC with a small transmission to observe the vibronic emission. For higher Tm^{3+} doping, a lower inversion is needed to overcome the losses and broad and flat gain spectra at long wavelengths are observed. It can be also interpreted as the effect of stronger reabsorption losses. For crystals with low Tm^{3+} doping (as for $MgWO_4$), a "bandpass" OC is required to suppress the oscillations at shorter wavelengths corresponding to a higher gain. To date, the longest vibronic emission wavelength was achieved from a 3 at.% Tm:KLuW crystal, 2109-2133 nm, corresponding to the highest output power of 1.17 W [41]. The highest slope efficiency (η = 61%) has been observed for a 12 at.% Tm:BaY_2F_8 laser emitting at 1978-2030 nm [45].

6. Conclusions

The monoclinic $MgWO_4$ crystal is a promising host for Tm^{3+} doping which will enable the development of efficient, broadly tunable and ultrashort-pulse mode-locked lasers emitting above 2 μm. This is determined by (i) the strong crystal field promoted by the difference of ionic radii of the dopant Tm^{3+} and passive Mg^{2+} ions leading to a large Stark splitting of the ground-state, $^3H_6$, (633 cm^{-1}), (ii) high transition cross-sections for polarized light, and (iii) attractive thermal properties, namely high thermal conductivity and positive thermal lens for the principal N_g- and N_p-cuts. According to the analysis of the Stark splitting of Tm^{3+} in $MgWO_4$ compared for various hosts, Tm:$MgWO_4$ is considered as an unique material combining very broad spectral bands extending above 2 μm with naturally polarized laser output. In the present work, we demonstrated, for the first time, wide tuning of the Tm:$MgWO_4$ laser (1897-2062 nm) and vibronic laser operation reaching even longer wavelengths up to 2093 nm. Operation above 2 μm is a prerequisite for achieving sub-100 fs pulses from ML solid-state lasers in this wavelength range because it helps to avoid air absorption and dispersion effects. The alternative Ho-lasers which normally operate also slightly above 2 μm exhibit more structured gain profiles compared to their Tm counterparts.

Further improvement of output performance of the Tm:$MgWO_4$ lasers can be performed in several directions. Regarding the power scaling and the enhancement of the laser efficiency in CW regime, higher Tm^{3+} doping concentrations are desirable. Power scaling will require direct measurements of the thermo-optical properties of Tm:$MgWO_4$ (thermal lensing and thermo-optic coefficients). To increase the slope efficiency, a spectroscopic study of the Tm^{3+}-Tm^{3+} cross-relaxation that is known to be very efficient in monoclinic double tungstates is required. Achieving high Tm^{3+} concentrations will require a clarification of the role of Na^+ ions in the doping mechanism. Regarding the vibronic and wavelength-tunable operation, experiments with spectrally-selective laser mirrors are expected to extend the emission range up to ~2.1 μm.

Acknowledgments

This work was supported by the National Natural Science Foundation of China (projects No. 11404332, No. 61575199, No. 21427801); Key Project of Science and Technology of Fujian Province (2016H0045); the Strategic Priority Research Program of the Chinese Academy of Sciences (No. XDB20000000); the National Key Research and Development Program of China (No. 2016YFB0701002); the China Scholarship Council (CSC, No. 201504910418 and No. 201504910629); the Instrument Project of Chinese Academy of Sciences (No. YZ201414); Spanish Government (No. MAT2016-75716-C2-1-R, No. (AEI/FEDER,UE), No. TEC 2014-55948-R) and Generalitat de Catalunya (No. 2014SGR1358). F.D. acknowledges additional support through the ICREA academia award 2010ICREA-02 for excellence in research. P. L.

acknowledges financial support from the Government of the Russian Federation (Grant No. 074-U01) through ITMO Post-Doctoral Fellowship scheme.

References

[1] V. Petrov, M. C. Pujol, X. Mateos, Ò. Silvestre, S. Rivier, M. Aguiló, R. M. Solé, J. H. Liu, U. Griebner, F. Díaz, Growth and properties of $KLu(WO_4)_2$, and novel ytterbium and thulium lasers based on this monoclinic crystalline host, Laser Photon. Rev. 1 (2007) 179-212.

[2] J. M. Cano-Torres, M. Rico, X. Han, M. D. Serrano, C. Cascales, C. Zaldo, V. Petrov, U. Griebner, X. Mateos, P. Koopmann, C. Kränkel, Comparative study of crystallographic, spectroscopic, and laser properties of Tm^{3+} in $NaT(WO_4)_2$ (T = La, Gd, Y, and Lu) disordered single crystals, Phys. Rev. B 84 (2011) 174207-1–15.

[3] P. A. Loiko, V. E. Kisel, N. V. Kondratuk, K. V. Yumashev, N. V. Kuleshov, A. A. Pavlyuk, 14 W high-efficiency diode-pumped cw $Yb:KGd(WO_4)_2$ laser with low thermo-optic aberrations, Opt. Mater. 35 (2013) 582-585.

[4] J. M. Serres, X. Mateos, P. Loiko, K. Yumashev, N. Kuleshov, V. Petrov, U. Griebner, M. Aguiló, F. Díaz, Diode-pumped microchip $Tm:KLu(WO_4)_2$ laser with more than 3 W of output power, Opt. Lett. 39 (2014) 4247-4250.

[5] U. Griebner, S. Rivier, V. Petrov, M. Zorn, G. Erbert, M. Weyers, X. Mateos, M. Aguiló, J. Massons, F. Díaz, Passively mode-locked $Yb:KLu(WO_4)_2$ oscillators, Opt. Express 13 (2005) 3465-3470.

[6] A. García-Cortes, J.M. Cano-Torres, M.D. Serrano, C. Cascales, C. Zaldo, S. Rivier, X. Mateos, U. Griebner, V. Petrov, Spectroscopy and lasing of Yb-doped $NaY(WO_4)_2$: Tunable and femtosecond mode-locked laser operation, IEEE J. Quantum Electron. 43 (2007) 758-764.

[7] M. S. Gaponenko, P. A. Loiko, N. V. Gusakova, K. V. Yumashev, N. V. Kuleshov, and A. A. Pavlyuk, Thermal lensing and microchip laser performance of N_g-cut $Tm^{3+}:KY(WO_4)_2$ crystal, Appl. Phys. B 108 (2012) 603-607.

[8] A. A. Kaminskii, H. J. Eichler, K. Ueda, N. V. Klassen, B. S. Redkin, L. E. Li, J. Findeisen, D. Jaque, J. García-Sole, J. Fernández, R. Balda, Properties of Nd^{3+}-doped and undoped tetragonal $PbWO_4$, $NaY(WO_4)_2$, $CaWO_4$, and undoped monoclinic $ZnWO_4$ and $CdWO_4$ as laser-active and stimulated Raman scattering-active crystals, Appl. Opt. 38 (1999) 4533-4547.

[9] A. Lupei, V. Lupei, C. Gheorghe, L. Gheorghe, A. Achim, Multicenter structure of the optical spectra and the charge-compensation mechanisms in $Nd:SrWO_4$ laser crystals, J. Appl. Phys. 104 (2008) 083102-1–7.

[10] H.P. Barbosa, I.G. Silva, M.C.F. Felinto, E.E. Teotonio, O.L. Malta, H.F. Brito, Photoluminescence of single-phased white light emission materials based on simultaneous Tb^{3+}, Eu^{3+} and Dy^{3+} doping in $CaWO_4$ matrix, J. Alloys Compd. 696 (2017) 820-827.

[11] W. Xu, Y. Cui, Y. Hu, L. Zheng, Z. Zhang, W. Cao, Optical temperature sensing in Er^{3+}-Yb^{3+} codoped $CaWO_4$ and the laser induced heating effect on the luminescence intensity saturation, J. Alloys Compd. 726 (2017) 547-555.

[12] C. Zhang, J. Zhang, Y. Li, J. Zhao, W. Wei, R. Yao, G. Jia, S. Shen, Fabrication, characterization, and luminescence properties of highly uniform $PbWO_4$: Ln^{3+} (Ln = Tb, Eu, Dy, and Sm) hierarchical microspheres, J. Alloys Compd. 698 (2017) 33-38.

[13] E. Cavalli, A. Belletti, M. G. Brik, Optical spectra and energy levels of the Cr^{3+} ions in MWO_4 (M = Mg, Zn, Cd) and $MgMoO_4$ crystals, J. Phys. Chem. Solids 69 (2008) 29-34.
[14] X. Wang, Z. Fan, H. Yu, H. Zhang, and J. Wang, Characterization of $ZnWO_4$ Raman crystal, Opt. Mater. Express 7 (2017) 1732-1744.
[15] P. Becker, L. Bohatý, H. J. Eichler, H. Rhee, A. A. Kaminskii, High-gain Raman induced multiple Stokes and anti-Stokes generation in monoclinic multiferroic $MnWO_4$ single crystals, Laser Phys. Lett. 4 (2007) 884-889.
[16] M.A. Prosnikov, V.Y. Davydov, A.N. Smirnov, M.P. Volkov, R.V. Pisarev, P. Becker, L. Bohatý, Lattice and spin dynamics in a low-symmetry antiferromagnet NiWO4, Phys. Rev. B 96 (2017) 014428.
[17] V. B. Kravchenko, Crystal structure of the monoclinic form of magnesium tungstate $MgWO_4$, J. Struct. Chem. 10 (1969) 139-140.
[18] P. Yadav, S.K. Rout, E. Sinha, Correlation between optical properties and environmental parameter of $ZnWO_4$ ceramic using complex chemical bond theory, J. Alloys Compd. 726 (2017) 1014-1023.
[19] M. Kumar, Y.H. Lee, M.S. Kim, D.I. Jeong, B.K. Kang, D.H. Yoon, Morphology-controlled synthesis of 3D flower-like $NiWO_4$ microstructure via surfactant-free wet chemical method, J. Alloys Compd. doi: 10.1016/j.jallcom.2018.04.114 (2018).
[20] A.C. Catto, T. Fiorido, E.L. Souza, W. Avansi Jr, J. Andres, K. Aguir, E. Longo, L.S. Cavalcante, L.F. da Silva, Improving the ozone gas-sensing properties of $CuWO_4$ nanoparticles, J. Alloys Compd. 748 (2018) 411-417.
[21] V. B. Mikhailik, H. Kraus, V. Kapustyanyk, M. Panasyuk, P. Yu, V. Tsybulskyi, L. Vasylechko, Structure, luminescence and scintillation properties of the $MgWO_4$–$MgMoO_4$ system, J. Phys.: Cond. Matter 20 (2008) 365219-1–8.
[22] F. A. Danevich, D. M. Chernyak, A. M. Dubovik, B. V. Grinyov, S. Henry, H. Kraus, V. M. Kudovbenko, V. B. Mikhailik, L. L. Nagornaya, R. B. Podviyanuk, O. G. Polischuk, I. A. Tupitsyna, Y. Y. Vostretsov, $MgWO_4$ – A new crystal scintillator, Nucl. Instrum. Meth. A 608 (2009) 107-115.
[23] L. Li, Y. Yu, G. Wang, L. Zhang, Z. Lin, Crystal growth, spectral properties and crystal field analysis of Cr^{3+}:$MgWO_4$, Cryst. Eng. Comm. 15 (2013) 6083-6089.
[24] L. Zhang, W. Chen, J. Lu, H. Lin, L. Li, G. Wang, G. Zhang, Z. Lin, Characterization of growth, optical properties, and laser performance of monoclinic Yb:$MgWO_4$ crystal, Opt. Mater. Express 6 (2016) 1627-1634.
[25] J. Lu, H. Lin, G. Zhang, B. Li, L. Zhang, Z. Lin, Y.-F. Chen, V. Petrov, W. Chen, Direct generation of an optical vortex beam from a diode-pumped Yb:$MgWO_4$ laser, Laser Phys. Lett. 14 (2017) 085807-1-6.
[26] H. Lin, G. Zhang, L. Zhang, Z. Lin, F. Pirzio, A. Agnesi, V. Petrov, W. Chen, Continuous-wave and SESAM mode-locked femtosecond operation of a Yb:$MgWO_4$ laser, Opt. Express 25 (2017) 11827-11832.
[27] L. Zhang, H. Lin, G. Zhang, X. Mateos, J. M. Serres, M. Aguiló, F. Díaz, U. Griebner, V. Petrov, Y. Wang, P. Loiko, E. Vilejshikova, K. Yumashev, Z. Lin, W. Chen, Crystal growth,

optical spectroscopy and laser action of Tm^{3+}-doped monoclinic magnesium tungstate, Opt. Express 25 (2017) 3682-3693.

[28] P. Loiko, J. M. Serres, X. Mateos, M. Aguiló, F. Díaz, L. Zhang, Z. Lin, H. Lin, G. Zhang, K. Yumashev, V. Petrov, U. Griebner, Y. Wang, S. Y. Choi, F. Rotermund, W. Chen, Monoclinic Tm^{3+}:$MgWO_4$: a promising crystal for continuous-wave and passively Q-switched lasers at ~2 μm, Opt. Lett. 42 (2017) 1177-1180.

[29] L. Zhang, Y. Huang, S. Sun, F. Yuan, Z. Lin, and G. Wang, Thermal and spectral characterization of Cr^{3+}:$MgWO_4$ – a promising tunable laser material, J. Lumin. 169, Part A (2016) 161-164.

[30] Y. Wang, W. Chen, M. Mero, L. Zhang, H. Lin, Z. Lin, G. Zhang, F. Rotermund, Y. J. Cho, P. Loiko, X. Mateos, U. Griebner, V. Petrov, Sub-100 fs Tm:$MgWO_4$ laser at 2017 nm mode locked by a graphene saturable absorber, Opt. Lett. 42 (2017) 3076-3079.

[31] L. N. Limarenko, A. E. Nosenko, M. V. Pashkovski, D. L. Futorski, The effect of structural defects on the physical properties of tungstates (Vyscha Shkola, Lviv, 1978) [In Russian].

[32] A. N. Winchell, G. Winchell, The microscopical characters of artificial inorganic solid substances: Optical properties of artificial minerals (McCrone Research Institute, Chicago, 1989).

[33] Ò. Silvestre, M. C. Pujol, M. Rico, F. Güell, M. Aguiló, F. Díaz, Thulium doped monoclinic $KLu(WO_4)_2$ single crystals: growth and spectroscopy, Appl. Phys. B 87 (2007) 707-716.

[34] A. A. Kornienko, E. B. Dunina, L. A. Fomicheva, Determination of odd-symmetry crystal-field parameters from optical spectra, Opt. Spectr. 116 (2014) 683-690.

[35] A. A. Kornienko, E. B. Dunina, Dependence of the Stark structure on the energies of the multiplets, JETP Lett. 59 (1994) 412-412.

[36] A. A. Kornienko, E. B. Dunina, A. A. Kaminskii, Influence of the interconfigurational interaction on the crystal field of Ln^{3+} ions, J. Exp. Theor. Phys. 89 (1999) 1130-1137.

[37] P. H. Haumesser, R. Gaumé, B. Viana, E. Antic-Fidancev, D. Vivien, Spectroscopic and crystal-field analysis of new Yb-doped laser materials, J. Phys.: Cond. Matter 13 (2001) 5427-5447.

[38] W. T. Carnall, P. R. Fields, K. Rajnak, Electronic energy levels in the trivalent lanthanide aquo ions. I. Pr^{3+}, Nd^{3+}, Pm^{3+}, Sm^{3+}, Dy^{3+}, Ho^{3+}, Er^{3+}, and Tm^{3+}, J. Chem. Phys. 49 (1968) 4424-4442.

[39] S. A. Payne, L. L. Chase, L. K. Smith, W. L. Kway, W. F. Krupke, Infrared cross-section measurements for crystals doped with Er^{3+}, Tm^{3+}, and Ho^{3+}, IEEE J. Quantum Electron. 28 (1992) 2619-2630.

[40] B. Aull, H. Jenssen, Vibronic interactions in Nd:YAG resulting in nonreciprocity of absorption and stimulated emission cross sections, IEEE J. Quantum Electron. 18 (1982) 925-930.

[41] P. Loiko, X. Mateos, S. Y. Choi, F. Rottermund, J. M. Serres, M. Aguiló, F. Díaz, K. Yumashev, U. Griebner, V. Petrov, Vibronic thulium laser at 2131 nm Q-switched by single-walled carbon nanotubes, J. Opt. Soc. Am. B. 33 (2016) D19-D27.

[42] X. Mateos, P. Loiko, J.M. Serres, K. Yumashev, U. Griebner, V. Petrov, M. Aguiló, F. Díaz, Efficient micro-lasers based on highly-doped monoclinic double tungstates, IEEE J. Quantum Electron. 53 (2017) 1700110-1-10.
[43] P. A. Loiko, J. M. Serres, X. Mateos, M. P. Demesh, A. S. Yasukevich, K. V. Yumashev, V. Petrov, U. Griebner, M. Aguiló, F. Díaz, Spectroscopic and laser characterization of Yb,Tm:KLu$(WO_4)_2$ crystal, Opt. Mater. 51 (2016) 223-231.
[44] P. Loiko, J. M. Serres, X. Mateos, S. Tacchini, M. Tonelli, S. Veronesi, D. Parisi, A. Di Lieto, K. Yumashev, U. Griebner, V. Petrov, Comparative spectroscopic and thermo-optic study of Tm:Li*Ln*F_4 (*Ln* = Y, Gd, and Lu) crystals for highly-efficient microchip lasers at ~2 μm, Opt. Mater. Express 7 (2017) 844-854.
[45] F. Cornacchia, D. Parisi, C. Bernardini, A. Toncelli, M. Tonelli, Efficient, diode-pumped Tm^{3+}:BaY_2F_8 vibronic laser, Opt. Express 12 (2004) 1982-1989.

List of figure captions

Fig. 1. Structure of $MgWO_4$: (a) fragment of the structure within a unit-cell; (b,c) linkages of the [MgO_6] and [WO_6] polyhedra (*green* and *violet*, respectively) in projection onto the (b) ***b-c*** and (c) ***a-c*** planes.

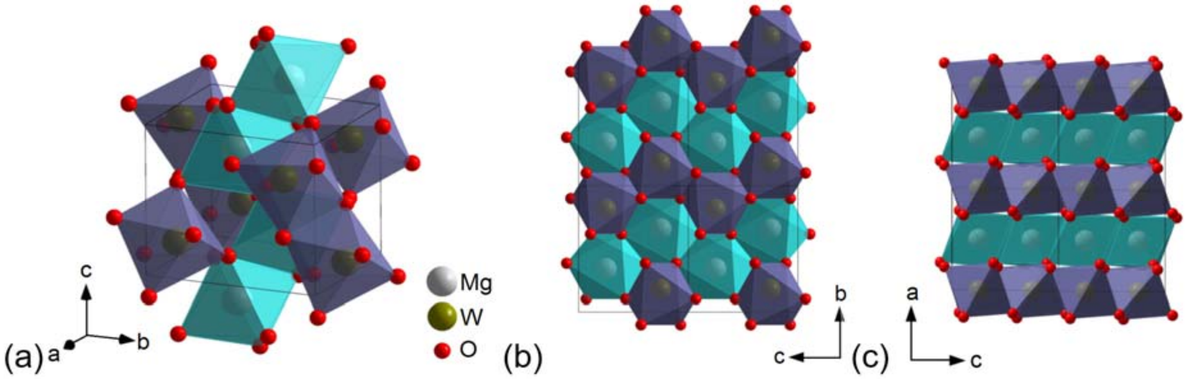

Fig. 2. Mutual orientation of the crystallographic (***a***, ***b***, ***c***) and the optical indicatrix (N_p, N_m, N_g) axes in Tm:$MgWO_4$.

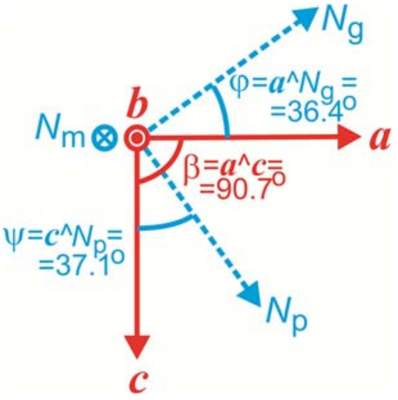

Fig. 3. (a-f) Low-temperature (6 K) absorption spectra of the Tm:$MgWO_4$ crystal for N_g and N_m light polarizations; "+" indicates the transitions to the Stark sub-levels.

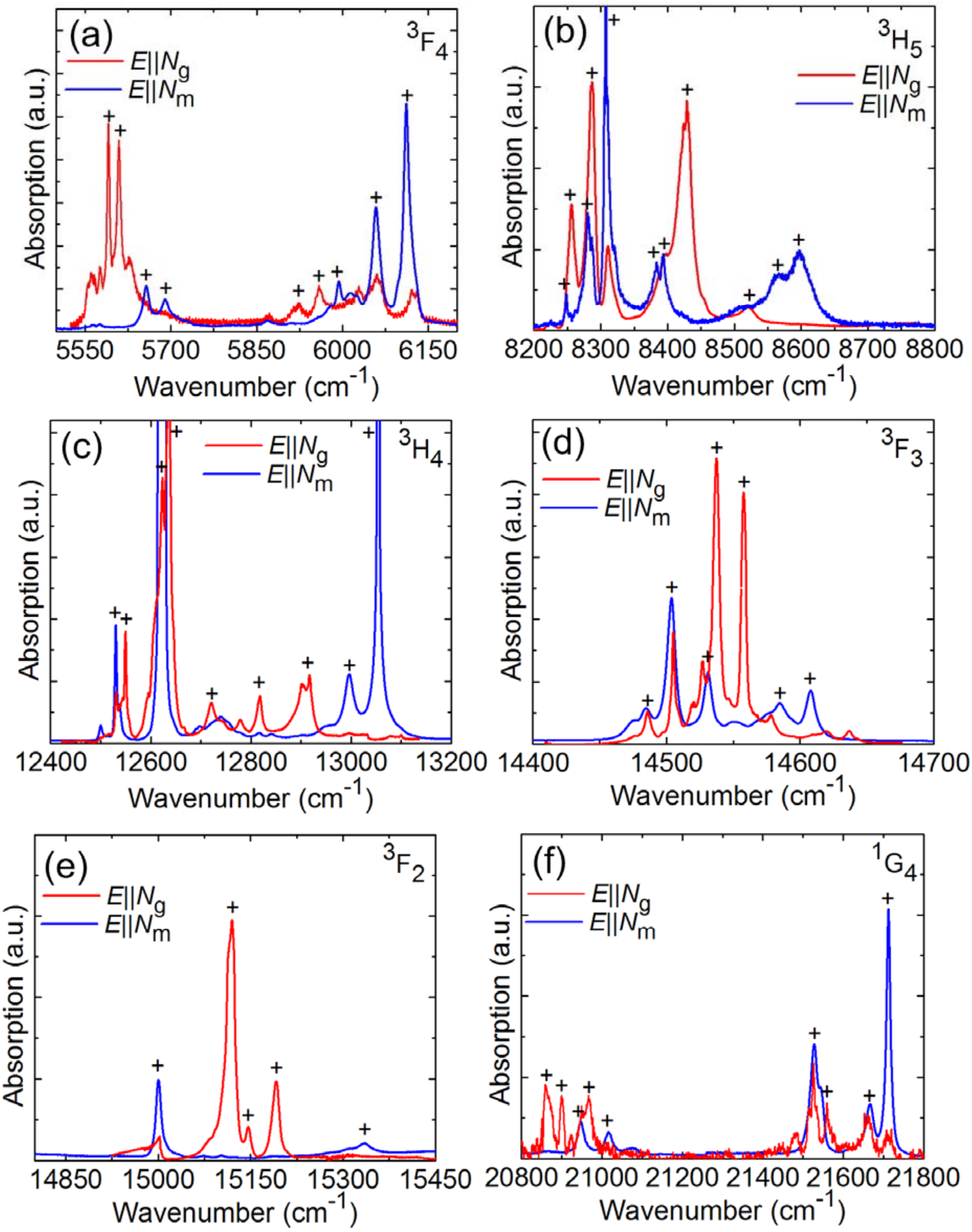

Fig. 4. Low-temperature (6 K) luminescence spectra of the $Tm:MgWO_4$ crystal for N_g and N_m light polarizations: the $^3H_4 \rightarrow {}^3H_6$ (a) and $^3F_4 \rightarrow {}^3H_6$ (b) transitions; "+" indicates the transitions to the Stark sub-levels. The excitation wavelength is 802 nm.

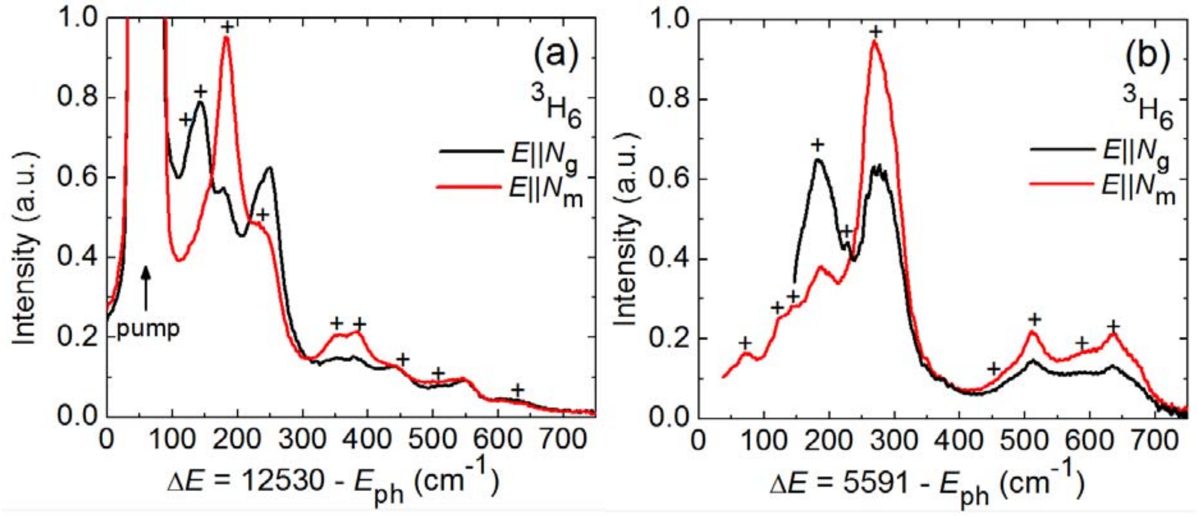

Fig. 5. (a) Scheme of the energy-levels of Tm^{3+} in $MgWO_4$ indicating the relevant spectroscopic processes (CR – cross-relaxation, NR – non-radiative relaxation, ETU – energy-transfer upconversion, ESA – excited-state absorption, UCL – upconversion luminescence); (b) comparison of the Stark splitting of the ground-state, $^3H_6$, and the upper laser level, $^3F_4$, of Tm^{3+} in the monoclinic $MgWO_4$, KLuW [26] and tetragonal NaGdW [2] crystals, $Z_{1(2)}$ are the partition functions. *Dashed arrows* indicate the zero phonon line transitions, *solid arrows* – electronic transitions corresponding to the longest wavelength.

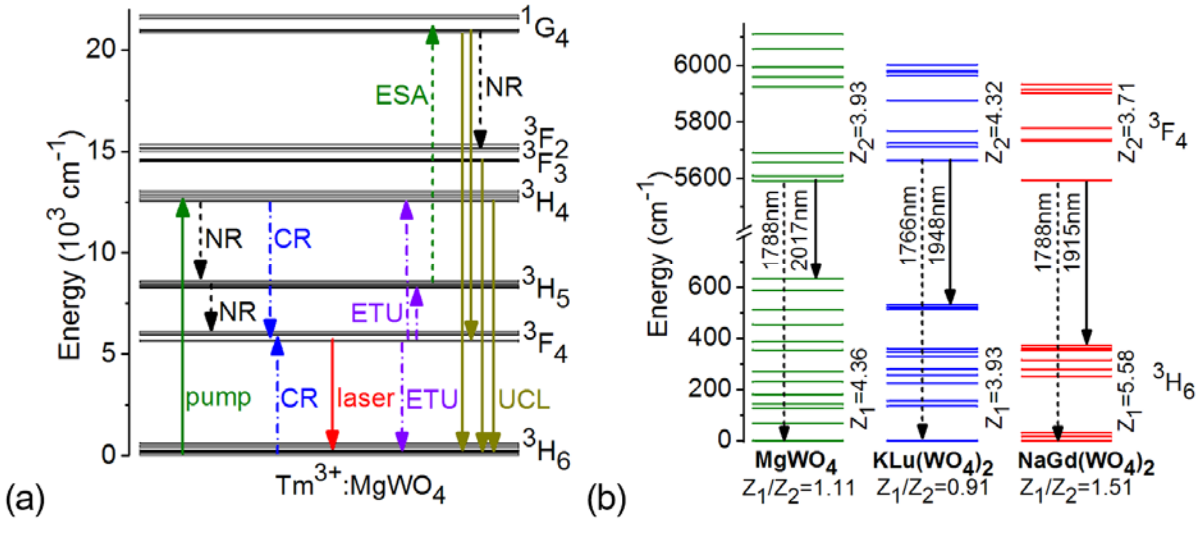

Fig. 6. Analysis of the crystal-field splitting for Tm^{3+} ions in various hosts: (a) a barycenter plot (barycenter energy ‹*E*› for the $^3F_4$ upper laser level vs. ‹*E*› for the $^3H_6$ ground-state): *symbols* – experimental data, *line* – their linear fit; (b) minimum energy E_{min} corresponding to the purely electronic transition $^3F_4 \rightarrow {}^3H_6$ vs. the total Stark spitting ΔE of the $^3H_6$ ground-state. Crystals acronyms: YAB = $Y_3Al(BO_3)_4$, YLF = $LiYF_4$, REAG = $RE_3Al_5O_{12}$, REGG = $RE_3Ga_5O_{12}$.

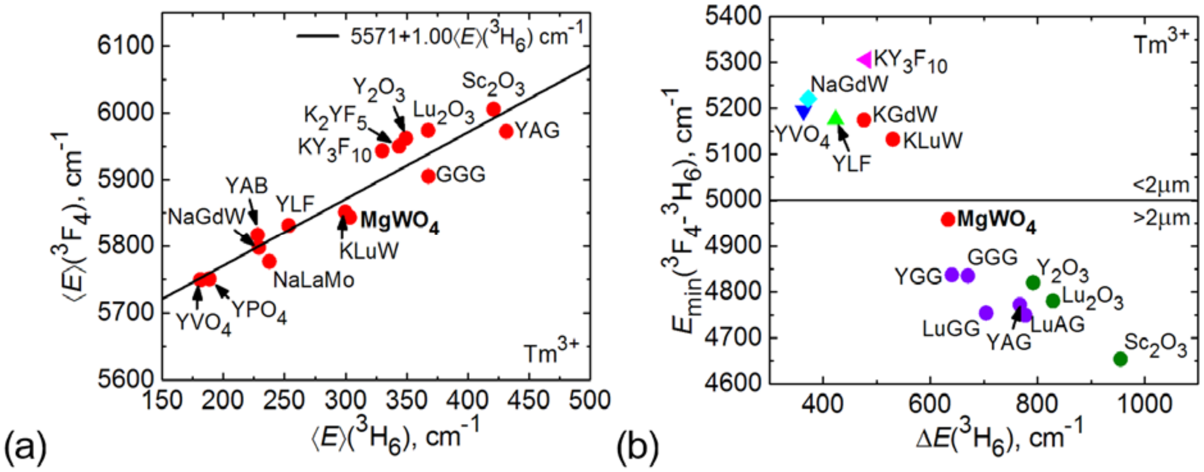

Fig. 7. Spectroscopy of the $^3F_4 \rightarrow {}^3H_6$ transition of Tm^{3+} in $MgWO_4$ for N_m light polarization: (a) absorption, σ_{abs}, and stimulated-emission, σ_{SE}, cross-sections (as calculated with the F-L and RM methods) (b) gain cross-sections, $\sigma_g = \beta\sigma_{SE} - (1 - \beta)\sigma_{abs}$, $\beta = N(^3F_4)/N_{Tm}$ is the inversion ratio.

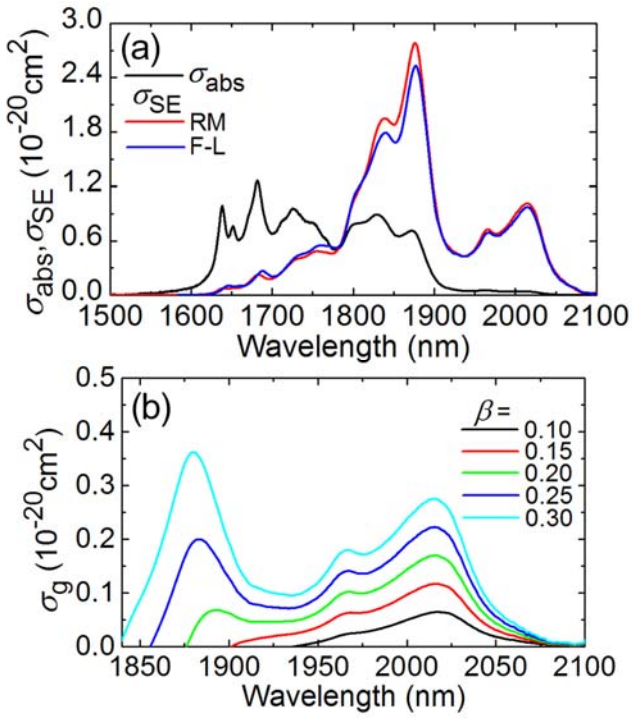

Fig. 8. Scheme of the wavelength-tunable Tm:MgWO$_4$ laser: M1, M2, M3 – highly-reflective mirrors, OC – output coupler.

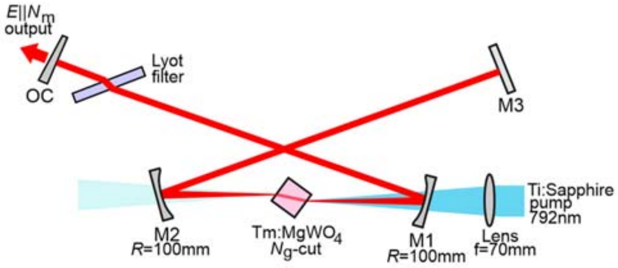

Fig. 9. CW Tm:MgWO$_4$ (N_g-cut) laser, Ti:Sapphire laser-pumped: (a,b) laser operation with different OCs, (a) input-output dependences, η – slope efficiency, (b) typical laser emission spectra measured at the maximum P_{abs}; (c) comparison of the tuning curves for Tm:MgWO$_4$ for N_m-polarization (T_{OC} = 1.5%, at P_{abs} = 1.6 W) and N_g-cut 3.7 at.% Tm:KLuW for N_p-polarization (T_{OC} = 3%, at P_{abs} = 2.4 W) [1].

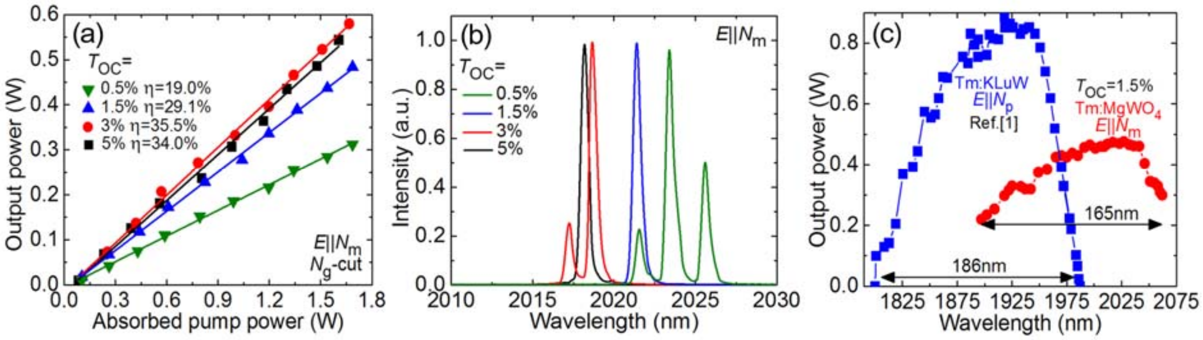

Fig. 10. Vibronic Tm:MgWO$_4$ (N_g- and N_p-cut) laser, diode-pumped: (a,b) input-output dependences, η – slope efficiency, (b) typical laser emission spectra measured at P_{abs} = 3.9 W (N_p-cut) and 1.3 W (N_g-cut crystal).

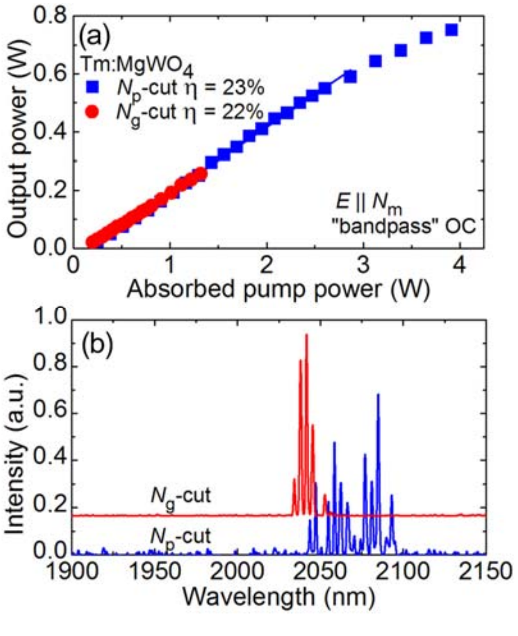

Table 1. Experimental and calculated energies of the Stark sub-levels of Tm^{3+} in $MgWO_4$ crystal.

$^{2S+1}L_J$	E_{exp}	E_{calc1}	E_{calc2}	ΔE_{calc2}	$^{2S+1}L_J$	E_{exp}	E_{calc1}	E_{calc2}	ΔE_{calc2}
$^3H_6$					$^3H_4$				
1	0	-24.0	16.6	-16.6	34	12530	12536.0	12534.2	-4.2
2	68	14.5	48.8	19.2	35	12549	12563.1	12536.0	13.0
3	126	62.4	105.1	20.9	36	12623	12643.4	12641.3	-18.3
4	143	76.7	124.7	18.3	37	12636	12649.1	12662.0	-26.0
5	181	173.3	203.2	-22.2	38	12721	12732.9	12743.8	-22.8
6	230	244.4	215.8	14.2	39	12817	12777.5	12782.6	34.4
7	270	288.2	287.4	-17.4	40	12903	12918.2	12909.5	-6.5
8	354	315.7	331.8	22.2	41	12996	12972.8	13003.0	-7.0
9	386	383.0	361.8	24.2	42	13054	13048.0	13049.8	4.2
10	454	486.2	454.9	-0.9	$^3F_3$				
11	511	550.6	507.7	3.3	43	14485	14461.5	14456.7	28.3
12	587	644.3	601.4	-14.4	44	14504	14512.1	14502.7	1.3
13	633	657.0	616.4	16.6	45	14531	14517.1	14526.7	4.3
$^3F_4$					46	14537	14543.1	14528.9	8.1
14	5591	5587.9	5594.9	-3.9	47	14557	14580.1	14575.0	-18.0
15	5609	5628.4	5639.7	-30.7	48	14584	14618.7	14616.9	-32.9
16	5656	5649.4	5682.4	-26.4	49	14608	14631.5	14636.3	-28.3
17	5690	5668.4	5690.9	-0.9	$^3F_2$				
18	5924	5897.5	5902.4	21.6	50	15000	15066.9	15059.9	-59.9
19	5959	5937.7	5928.6	30.4	51	15119	15143.6	15125.3	-6.3
20	5994	5989.9	5953.9	40.1	52	15145	15155.9	15159.2	-14.2
21	6058	6053.0	6023.1	34.9	53	15192	15203.0	15193.0	-1.0
22	6111	6114.1	6107.1	3.9	54	15335	15268.1	15275.1	59.9
$^3H_5$					$^1G_4$				
23	8247	8197.3	8205.8	41.2	55	20858	20913.2	20850.3	7.7
24	8256	8234.4	8246.4	9.6	56	20897	20954.6	20890.0	7.0
25	8280	8245.9	8255.1	24.9	57	20946	21004.6	20969.3	-23.3
26	8286	8284.2	8289.0	-3.0	58	20968	21038.3	20988.2	-20.2
27	8310	8314.5	8308.7	1.3	59*	21017	21344.4	21304.0	-287.0
28	8383	8377.7	8371.8	11.2	60	21528	21471.2	21505.3	22.7
29	8393	8423.0	8407.1	-14.1	61	21560	21502.1	21559.5	0.5
30	8428	8510.1	8488.6	-60.6	62	21666	21610.1	21671.2	-5.2
31	8521	8566.8	8554.5	-33.5	63	21713	21657.8	21720.7	-7.7
32	8564	8620.9	8587.6	-23.6					
33	8597	8646.7	8638.2	-41.2	σ		*42.7*	*28.8*	

E_{exp} – experimental energy, E_{calc} – calculated one (1 – WCI, 2 – ICI approximations), $\Delta E_{calc} = E_{exp} - E_{calc}$ (all values are in cm^{-1}), σ – standard deviation between E_{exp} and E_{calc}.

Table 2. Calculated parameters of the Hamiltonian of the crystal field for Tm^{3+} in $MgWO_4$ crystal.

WCI model		ICI model			
	in cm^{-1}		in cm^{-1}		
B^2_0	145	B^2_0	164	$S^1_0\times10^4$	-162
B^2_2	-9	B^2_2	-28	$S^3_0\times10^4$	298
iB^2_2	-27	iB^2_2	-41	$S^5_0\times10^4$	1112
B^4_0	921	B^4_0	730	$\gamma_{\sigma f}\times10^4$	-637
B^4_2	-648	B^4_2	-149	$\gamma_{\pi f}\times10^4$	374
iB^4_2	1150	iB^4_2	898		
B^4_4	-122	B^4_4	-36		
iB^4_4	-16	iB^4_4	257		
B^6_0	-177	B^6_0	-315		
B^6_2	-513	B^6_2	-765		
iB^6_2	-808	iB^6_2	-610		
B^6_4	-270	B^6_4	-378		
iB^6_4	-270	iB^6_4	-178		
B^6_6	-306	B^6_6	-216		
iB^6_6	-9	iB^6_6	126		

i – imaginary, $S^p_0 = B^p_0(d)/\Delta_d$.

Table 3. Output characteristics of vibronic thulium lasers reported so far.

Crystal	Tm doping	P_{out}, W	λ_L, nm	η, %	OC	Ref.
Tm:$MgWO_4$	0.89 at.%	0.75	2043-2093	23	bandpass	This work
Tm:$KLu(WO_4)_2$	3 at.%	1.17	2109-2133	39	bandpass	[34]
	15 at.%	0.59	2005-2045	51	1.5%	[35]
Yb,Tm:$KLu(WO_4)_2$	6 at.%	0.11	2081-2092	8	0.05%	[36]
Tm:$LiYF_4$	8 at.%	0.38	2026-2044	31	bandpass	[37]
Tm:BaY_2F_8	12 at.%	0.29	1978-2030	61	0.5%	[38]